ACS APPLIED MATERIALS & INTERFACES

www.acsami.org Research Article

Interfacial Thermal Conductance between Monolayer WSe_2 and SiO_2 under Consideration of Radiative Electron−Hole Recombination

Nicholas Hunter,[‖] Nurul Azam,[‖] Hamidreza Zobeiri,[‖] Ridong Wang, Masoud Mahjouri-Samani,* and Xinwei Wang*

Cite This: *ACS Appl. Mater. Interfaces* 2020, 12, 51069−51081 Read Online

ACCESS | Metrics & More | Article Recommendations

Downloaded via IOWA STATE UNIV on December 27, 2020 at 22:04:43 (UTC). See https://pubs.acs.org/sharingguidelines for options on how to legitimately share published articles.

ABSTRACT: This work reports the interfacial thermal conductance (G) and radiative recombination efficiency (β), also known as photoluminescence quantum yield (PL QY), of monolayer WSe_2 flakes supported by fused silica substrates via energy-transport state-resolved Raman (ET-Raman). This is the first known work to consider the effect of radiative electron−hole recombination on the thermal transport characteristics of single-layer transition-metal dichalcogenides (TMDs). ET-Raman uses a continuous-wave laser for steady-state heating as well as nanosecond and picosecond lasers for transient energy transport to simultaneously heat the monolayer flakes and extract the Raman signal. The three lasers induce distinct heating phenomena that distinguish the interfacial thermal conductance and radiative recombination efficiency, which can then be determined in tandem with three-dimensional (3D) numerical modeling of the temperature rise from respective laser irradiation. For the five samples measured, G is found to range from 2.10 ± 0.14 to 15.9 ± 5.0 MW m^{-2} K^{-1} and β ranges from 36 ± 6 to 65 ± 7%. These values support the claim that interfacial phenomena such as surface roughness and two-dimensional (2D) material−substrate bonding strength play critical roles in interfacial thermal transport and electron−hole recombination mechanisms in TMD monolayers. It is also determined that low-level defect density enhances the radiative recombination efficiency of single-layer WSe_2.

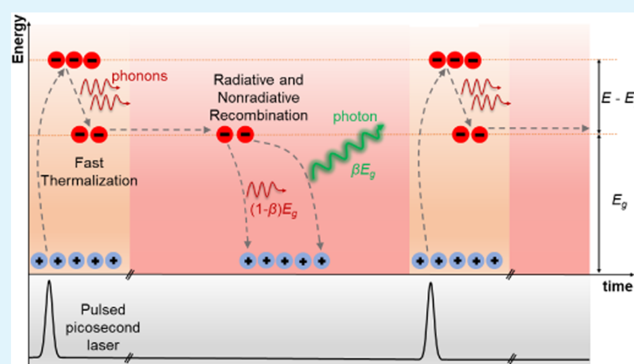

KEYWORDS: *interfacial thermal conductance, radiative recombination efficiency, monolayer WSe_2, Raman spectroscopy, 2D materials*

INTRODUCTION

Transition-metal dichalcogenides (TMDs) two-dimensional (2D) materials are attracting significant research attention for their unique electrical and optical properties. Some of these remarkable properties include tunable bandgaps, large exciton binding energy, and strong photoluminescence (PL) as monolayers due to their indirect to direct bandgap transition as the 2D material thickness decreases to a single layer.[1−3] A wide range of potential applications exists for these novel 2D materials including integrated circuitry, optoelectronics, spintronics, and field-effect transistors.[4−7] The increased photoluminescence as monolayers makes TMDs particularly suitable for atomic-scale light-emission devices.[8]

Before 2D TMDs can be incorporated as reliable materials for modern technology needs and green energy solutions, a proper understanding of heat dissipation at the nanoscale is critical. The thermal resistance in nanoscale devices dictates overall performance and can severely limit the operation of electronic systems. In particular, the interfacial thermal conductance (G) between a 2D material and its substrate is subject to numerous factors such as surface roughness, compositional disorder, atomistic dislocations, and interfacial bonding.[9] The variability of interface phenomena and the atomic-level thickness of 2D TMDs make a precise characterization of interfacial thermal transport very difficult.

Researchers have employed optical, electrical, and computational techniques to study the interfacial thermal conductance between thin-film TMDs and substrates. Comparison of recent works reveals moderate to substantial discrepancies between the reported results. Yasaei et al.[10] used electrical thermometry and subsequent three-dimensional (3D) finite element analysis to characterize thermal transport across monolayer MoS_2 and SiO_2/Si substrates to conclude a thermal boundary conductance of 20.3−33.5 MW m^{-2} K^{-1}. For comparison, Zhang et al.[11] measured a thermal conductance to be of the order

Received: August 19, 2020
Accepted: October 14, 2020
Published: October 27, 2020

© 2020 American Chemical Society

https://dx.doi.org/10.1021/acsami.0c14990
ACS Appl. Mater. Interfaces 2020, 12, 51069−51081

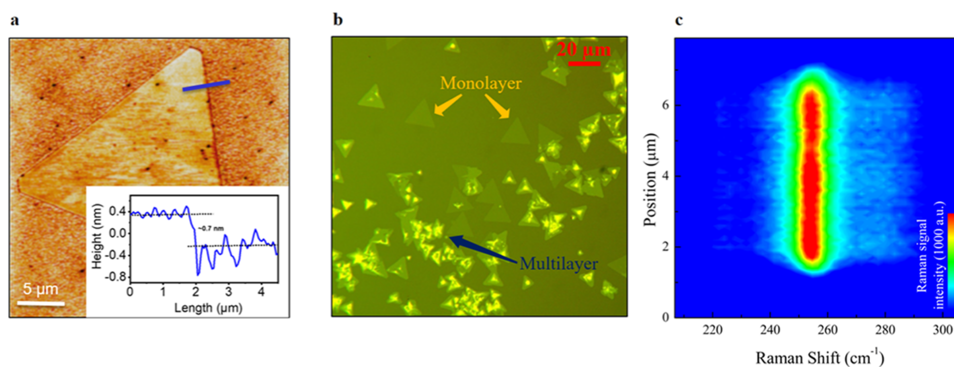

Figure 1. Images detailing the structural characterization of the WSe_2 monolayer samples. (a) AFM image of a single-monolayer flake with the accompanying line profile shows a sample height of ∼0.7 nm. Note the surface roughness transition from the WSe_2 area to the fused silica substrate; the fused silica demonstrates noticeably higher levels of surface roughness. (b) Optical image shows the representative monolayer samples, slightly pronounced from the underlying substrate. From the base of the triangular flake to the opposite vertex, the monolayers measure approximately 13 μm. The multilayer samples show more variation at the surface and appear brighter. (c) Raman measurements collected as a 1D line scan across the surface of a monolayer sample demonstrate the structural uniformity of WSe_2. The line scan was measured along an 8 μm distance with Raman measurements taken at 0.1 μm intervals. The constant Raman signal intensity during the line scan suggests uniform structural characteristics.

0.1−1 MW m^{-2} K^{-1} using a refined optothermal Raman technique on single and bilayer MoS_2 and $MoSe_2$. On the computational and theoretical side, the acoustic mismatch model (AMM),[12] diffuse mismatch model (DMM),[13] and molecular dynamics simulations[14] are commonly used to predict G. Correa et al.[15] developed a first-principles model for interfacial phonon transport to predict a larger G of $\sim 10^8$ W m^{-2} K^{-1} between monolayer MoS_2 and amorphous SiO_2 and proposed that large surface variation or sharp atomic-scale features between the sample and substrate decrease overall conductance across an interface. The 1−2 orders of magnitude difference for the reported G values of the MoS_2 monolayers suggest a need for more refined interfacial thermal conductance measurement techniques.

Raman-based thermal probing techniques using steady-state lasers are employed frequently to study thermal properties of 2D materials.[16−19] However, the optothermal Raman technique requires calibration of a Raman temperature coefficient and precise determination of laser absorption, both of which are subject to non-negligible error that could impact final experimental results. As thoroughly detailed by Xu et al.,[20] thermal expansion mismatch between the sample and substrate during calibration introduces stress distinct from the stress involved from laser heating during Raman probing. Therefore, relying on temperature coefficients determined during calibration may introduce unknown error when using Raman spectroscopy to measure the sample temperature change. Additionally, laser absorption measurements can be affected by interfacial spacing, which causes Raman intensity enhancement due to multiple reflections at the interface gap. Optical absorption measurements then become sample specific since interface spacing between the 2D material and substrate can vary depending on the thickness of the sample and preparation method.[21] Laser absorption coefficients are often estimated from models or borrowed from others' work introducing further uncertainty to Raman-based temperature measurements.[17,18]

The radiative recombination of electron−hole (e−h) pairs further complicates experimental measurements of interfacial thermal conductance. Because monolayer TMDs have a direct bandgap, laser-excited electrons in the conduction band have a probability of recombining radiatively with holes in the valence band (i.e., photon emission). This means that not all of the laser energy absorbed in the sample converts to thermal energy in the form of phonons or hot electrons.[22] This critical feature of monolayer TMDs has never been considered while studying interfacial conductance via Raman-based thermal probing with laser heating. A full physics understanding of local interface energy coupling requires consideration of the radiative recombination effect in single-layer TMD materials.

In this work, we report the interfacial thermal conductance of monolayer tungsten diselenide (WSe_2) on fused silica (SiO_2) substrates with consideration of radiative recombination physics. In recently published work, we have extensively detailed a novel technique, energy-transport state-resolved Raman (ET-Raman), that eliminates uncertainty introduced by laser absorption measurements and Raman temperature calibration required in most Raman-based thermal measurements. ET-Raman involves differentiating the thermal energy-transport mechanism for a sample under laser heating by changing laser sources from continuous-wave (CW) (steady state) to pulsed laser (transient heat conduction). Three lasers, continuous wave (CW), nanosecond (ns), and picosecond (ps), irradiate the monolayers to induce unique temperature rises after which a spectrometer measures the resulting Raman signals. The samples are initially at room temperature surrounded by ambient air conditions. Different laser powers are required from each laser to generate experimentally measurable Raman signal redshifts ($\Delta\omega$). Although different powers are used for each laser, the ET-Raman method employed only requires relative Raman signal redshift (i.e., temperature rise) information. This method eliminates the light interference effect at the interfacial gap as well as the need for a sample-dependent Raman temperature coefficient. ET-Raman also considers the radiative recombination effect in monolayer TMD thermal transport.

In this work, we use the CW (steady state) and ns (pulsed) lasers in conjunction with 3D numerical modeling to simulate temperature rises of the laser-heated sample area and determine the interfacial thermal conductance G. Once G is determined, we introduce the ps pulsed laser to determine the radiative recombination coefficient (β). Because the average excited carrier lifetime of monolayer WSe_2 is much longer than the picosecond pulse width (13 ps), no electron−hole pairs

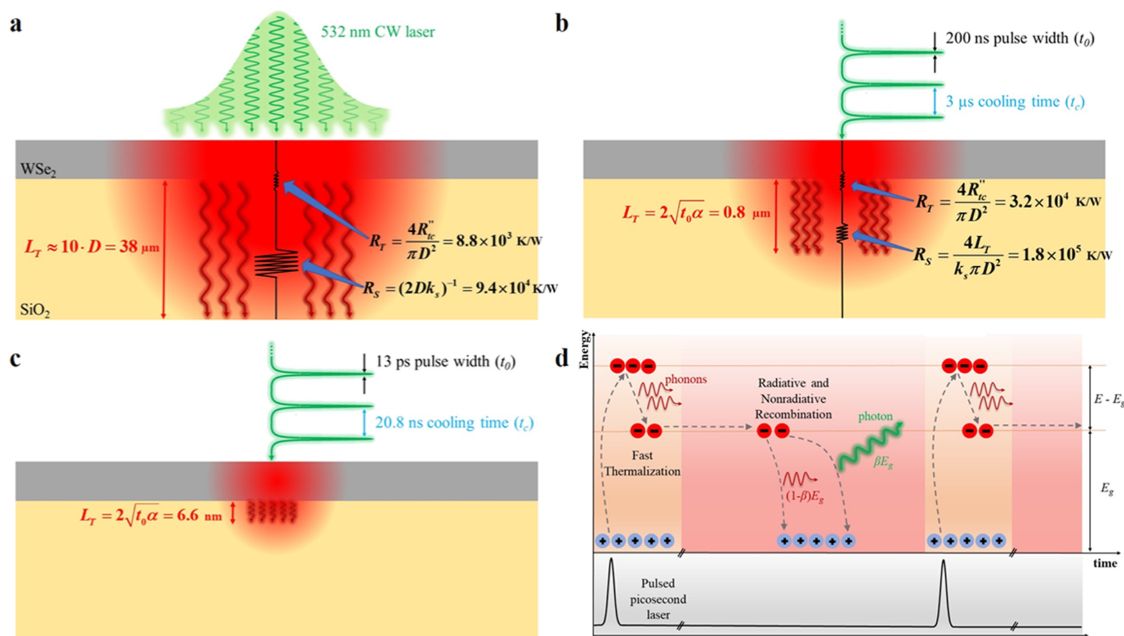

Figure 2. Steady-state and zero transport heat conduction in the WSe_2 2D monolayers using continuous-wave, nanosecond, and picosecond lasers. (a) In CW steady-state heating, substrate thermal resistance has a larger effect than total interface resistance. Using the appropriate shape factor for conduction heat transfer through a disk with diameter D on a semi-infinite medium, substrate resistance is calculated as $R_S = 1/(2Dk_s)$ where D = 3.8 μm is the diameter of the CW laser spot and k_s = 1.4 W m^{-2} K^{-1} is the substrate conductivity. Total interface resistance is calculated as $R_T = 4R''_{tc}/\pi D^2$. The thermal diffusion length L_T is estimated as 10× the laser spot diameter. (b) During nanosecond pulsed heating, the substrate resistance becomes more comparable to the interface resistance and is more sensitive to measurement. The substrate resistance is evaluated using $R_S = 4L_T/k_s\pi D^2$ where D = 2 μm for the nanosecond laser spot size and L_T is the ns heat diffusion length. This penetration into the substrate is approximately 800 nm, much larger than the sample thickness but smaller than the CW heat diffusion length. The ns R_T is evaluated using the same formula as the CW case but with the ns diameter. (c) For picosecond pulsed heating, L_T is only ∼7 nm. (d) Recombination physics in WSe_2 during pulsed picosecond laser heating. The short laser pulse does not involve e−h recombination. Direct phonon emission is the only source of thermal energy during this time. After the pulse, both nonradiative and radiative recombination occur with respective efficiencies of $(1 - \beta)$ and β.

have time to recombine during pulse heating. Thus, heating of the sample during the picosecond pulse only consists of thermal energy in the form of phonons during the fast thermalization process. By distinguishing multiple energy-transport states, two where radiative recombination occurs (CW and ns) and one where it does not (ps), the proportion of electron−hole pairs that recombine radiatively can be determined.

■ MATERIALS AND METHODS

Sample Preparation and Characterization. The 2D crystals were prepared by the laser-assisted synthesis technique (LAST),[23] where the high-quality monolayer WSe_2 crystals were directly synthesized from the stoichiometric powder. Stoichiometric WSe_2 powder was placed inside a custom-made graphite crucible (1.2 × 0.7 × 0.7 cm^3), and subsequently, a CW CO_2 laser with 10.6 μm wavelength was used to heat the graphite crucible to evaporate the WSe_2 powder. Transparent fused silica was used as the growth substrate. The substrate was placed face down on top of the graphite crucible at a 6 mm distance inside a 1-in. furnace tube. Due to chemically inert and low heat conductivity attributes, argon gas was used as the background gas to adjust the growth pressure to 150 Torr. Before starting the growth process, the furnace tube was vacuumed, followed by an argon flow to flush the residual remains of air molecules. After adjusting the furnace temperature to 800 °C, the growth process was initiated by irradiating the graphite crucible at 35 W laser power for 50 s. Right after finishing the irradiation process, the vacuum environment was kept active until the furnace was naturally cooled down to room temperature.

The LAST method produces high-quality WSe_2 monolayer flakes well suited for optothermal Raman measurements. Photoluminescence mapping and annular dark-field scanning transmission electron microscopy (ADF-STEM) imaging confirm the excellent quality and low-defect density of the synthesized crystals. This data can be found in the work of Azam et al.[23] Further information about the quality of the WSe_2 monolayer is expanded upon in later discussion. Atomic force microscopy (AFM) imaging measured the thickness of the monolayers to be approximately 0.7 nm (Figure 1a). The line profile in the AFM image shows a smooth surface on the WSe_2 monolayer relative to the fused silica substrate. Because the LAST method produces an abundance of monolayer as well as few-layered samples, the distinction between them is shown in Figure 1b. Monolayers exhibit a uniform surface and appear only slightly distinguished from the underlying substrate. The few-layered samples appear brighter and display more variation on their surfaces. Measured from the vertex to the opposite base of a triangular flake, the monolayer samples measure ∼13 μm across. To study the structural uniformity of the monolayers, Raman measurements were collected in a one-dimensional (1D) line scan across the surface of a sample. As can be seen in Figure 1c, the Raman signal strength remains constant over the entire length of the sample, suggesting a high degree of structural uniformity.

Interface Thermal Characterization and Radiative Recombination Probing: Physics. In the ET-Raman technique, different energy-transport states (in spatial and time domains) are constructed. This is intended to differentiate physical transport processes in the material. In the past, we have used this technique to distinguish the in-plane heat conduction, interface thermal conduction, and in-plane hot carrier diffusion of supported and suspended 2D materials including MoS_2, $MoSe_2$, and WS_2.[24−28]

In this work, we construct three different energy-transport states in the time domain (steady, nanosecond, and picosecond) to explore the interface energy-transport and electron−hole recombination process. The first step in the ET-Raman process involves laser heating and Raman probing of the WSe_2 monolayers with a CW and ns laser, both

https://dx.doi.org/10.1021/acsami.0c14990
ACS Appl. Mater. Interfaces 2020, 12, 51069−51081

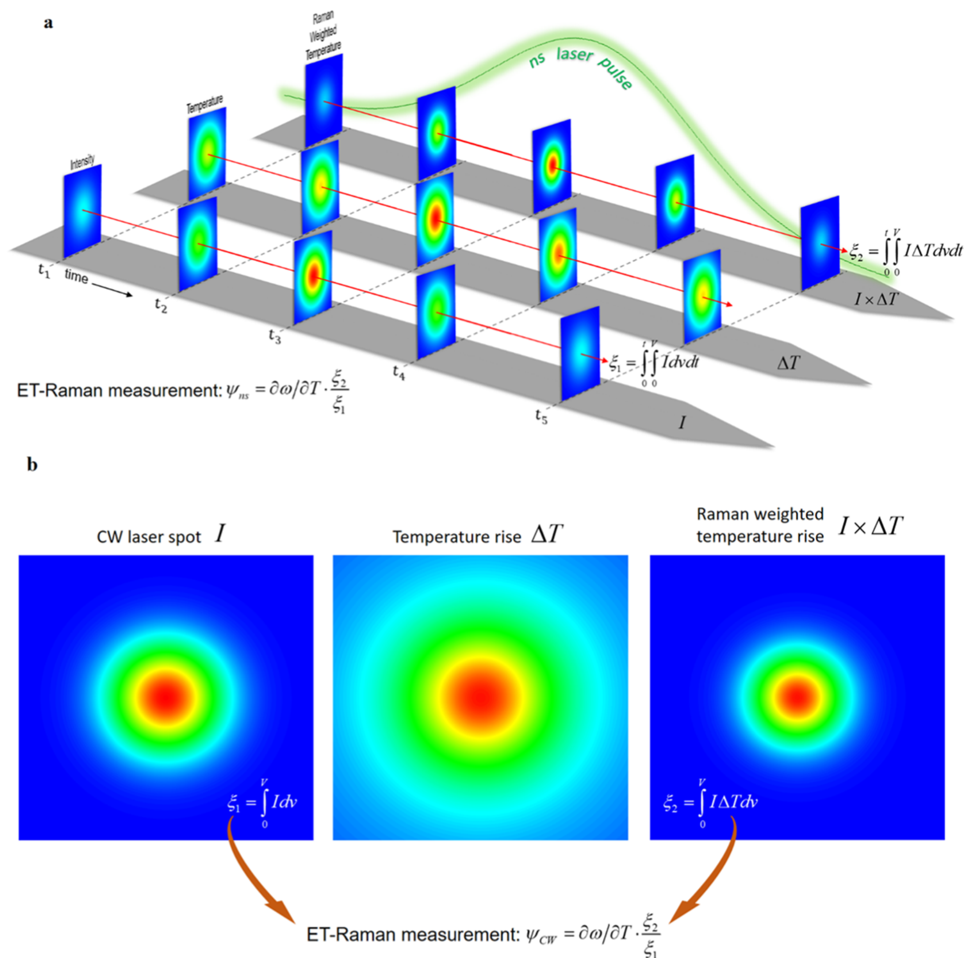

Figure 3. Illustration of the sample surface temperature and laser spot intensity that compose the Raman weighted temperature and subsequent Raman shift power coefficient ψ for the ns and CW laser heating and Raman probing. (a) Time progression of the laser spot intensity I, surface temperature ΔT, and corresponding Raman weighted temperature $I \times \Delta T$ during a single ns laser pulse. The intensity and Raman weighted temperatures are both shown as integrals over the spatial and time domain, ξ_1 and ξ_2, which are divided to represent the Raman shift coefficient ψ_{ns}. (b) Laser spot intensity and Raman weighted temperatures for the CW cases are simply integrated over the spatial domain. Their ratio determines the Raman shift power coefficient ψ_{CW}.

with the 532 nm wavelength (photon energy of E = 2.33 eV). A 20× objective lens focuses the laser beam on the sample. At this objective, the laser spot size covers most of the triangular crystal of the monolayer WSe_2. Therefore, the in-plane thermal diffusion outside of the laser heating area becomes negligible. The large laser spot size (r_o ~ 1.9 μm) relative to the atomically thin WSe_2 layer (~1 nm) also means that the cross-plane phonon transport at the interface dominates over the negligible in-plane heat conduction and hot carrier diffusion.[24]

The hot carrier diffusion length remains the same for all three laser heating scenarios and is evaluated using the formula $L = \sqrt{D\tau}$ where D = 2.2 $cm^2\ s^{-1}$ for hot carrier diffusivity and τ = 4 ns for hot carrier lifetime.[29] This estimate puts the hot carrier diffusion length in the order of 1 μm. Considering the recombination process during diffusion and the relatively large laser spot size, this hot carrier diffusion will have a negligible effect on the heat spreading in the in-plane direction.[28] The thermal diffusion length (L_T) for CW steady-state heating is essentially infinite but can be approximated in this case as 10× the laser spot diameter. In either case, this length is much larger than the atomically thin WSe_2 layer and allows us to assume uniform temperature distribution in the thickness direction (z-direction).

In the CW case, the laser irradiates a WSe_2 monolayer and causes steady-state heating. The laser power (P) gradually increases while the Raman signal is collected to study the temperature profile. Since the Raman shift location (ω) is redshifted with increasing laser power, we obtain a laser power differential we have called the Raman shift power coefficient (RSC): $\psi_{CW} = \partial\omega/\partial P$. The RSC is applied to the degenerate A_{1g} and $^1E_{2g}$ first-order Raman active modes of monolayer WSe_2 that appear as a single prominent peak around 250 cm^{-1} in the Raman spectrum.[30] It is important to note that this laser power differential is proportional to the laser absorption coefficient (α) and Raman temperature coefficient ($\partial\omega/\partial T$) and is also a function of substrate thermal resistance (R_S), interfacial thermal resistance (R''_{tc}), or equivalently G^{-1}. However, as stated previously, the ET-Raman technique eliminates the effects of laser absorption and Raman temperature coefficient, as will be explained in the upcoming section. Therefore, the remaining variables of interest become the already known substrate thermal resistance and the interfacial thermal resistance.

Under CW steady-state heating, because of the low thermal conductivity of fused silica, the accumulated heating of the substrate disproportionately impacts the overall thermal transport of the system. In other words, the substrate thermal resistance contributes to the measured temperature rise much more than the total interface resistance. Here, the substrate resistance is evaluated using the appropriate shape factor for conduction heat transfer through a disk with diameter D on a semi-infinite medium: $R_S = 1/(2Dk_s)$ where D is the laser spot diameter and k_s is the substrate thermal conductivity.[31] The total interface resistance is evaluated using $R_T = 4R''_{tc}/\pi D^2$ where

https://dx.doi.org/10.1021/acsami.0c14990
ACS Appl. Mater. Interfaces 2020, 12, 51069−51081

R''_{tc} is the interfacial thermal resistance per unit area. As shown in this paper, the interfacial resistance is in the order of 10^{-7} K m^2 W^{-1}. Thus, the substrate resistance is significantly larger than the total interface resistance by an order of magnitude: 9.4×10^4 and 8.8×10^3 K W^{-1}, respectively (see Figure 2a). This means that the R_T is only 9% of the R_S. Therefore, the interfacial conductance G contributes far less to the measured temperature change and has low sensitivity to meaningful measurement. The CW state serves as a reference state and will be used later in data processing to nullify the effects of laser absorption and Raman temperature coefficient.

In contrast to the CW steady-state laser heating, in the ns case, the substrate thermal resistance does not dominate the overall thermal transport of the system due to the smaller heat diffusion into the fused silica during pulse heating, as shown in Figure 2b. A nanosecond pulsed laser with a 300 kHz frequency repetition rate irradiates the sample. For a pulsed laser, the heat diffusion length into the substrate is estimated as $L_T = 2\sqrt{t_0\alpha}$ where t_0 = 200 ns is the laser pulse width and α is the thermal diffusivity of the substrate. The diffusion length value for fused silica under nanosecond pulsed laser heating is 0.8 μm. Under these conditions, the substrate thermal resistance is estimated as $R_S = 4L_T/k_s\pi D^2$ where D is the ns laser spot diameter (2 μm). Thus, the substrate resistance value is 1.8×10^5 K W^{-1}, which is more comparable to the total interface resistance value evaluated as 3.2×10^4 K W^{-1} (using the same equation for R_T as the CW case); in other words, R_T becomes 18% of R_S. To summarize, in the CW case, the substrate resistance effect is more pronounced and masks the presence of the total interface resistance. In the ns case, the total interface resistance influences the thermal transport of the system more prominently.

Like the CW case, laser power increases while the Raman signal is collected to obtain the nanosecond Raman shift coefficient (ψ_{ns}). At this point, we have two RSC's (ψ_{CW} and ψ_{ns}) representing the laser power differentials applied to Raman shift for two different heating mechanisms in the sample−substrate system. By taking their ratio, a new parameter is defined called the normalized Raman shift coefficient: $\Theta_1 = \psi_{ns}/\psi_{CW}$. This normalized parameter becomes a function of interfacial thermal resistance (i.e., conductance) alone since the Raman temperature coefficient and laser absorption are canceled out. A finite volume numerical simulation of the heat transfer in both CW and nanosecond cases computes theoretical temperature rises ΔT_{CW} and ΔT_{ns}. Equating the ratio of the temperature rises to the normalized RSC Θ_1 allows for precise determination of the interfacial thermal conductance.

Note that both temperatures rises are Raman intensity weighted averages, evaluated over the spatial domain for CW and the spatial−temporal domain for ns. Details of this discussion have been given in our past work.[24] Figure 3 illustrates the spatial and temporal components involved in the Raman weighted averages for both CW and ns cases. A single ns laser pulse exhibits a Gaussian intensity distribution, which must be integrated over space and time (denoted in Figure 3a as $\xi_1 = \int_0^t \int_0^V I \, dv \, dt$). The sample surface temperature multiplied by the weighted intensity values and then integrated over the time and space domain yields the Raman weighted temperature (denoted in the figure as $\xi_2 = \int_0^t \int_0^V I\Delta T \, dv \, dt$). The subsequent Raman weighted average value representing the experimental temperature rise during ns heating is related to the Raman shift power coefficient $\psi_{ns} = \partial\omega/\partial T \cdot \xi_2/\xi_1$. A similar mathematical treatment evaluated solely over the spatial domain for CW laser heating is shown in Figure 3b where $\xi_1 = \int_0^V I \, dv$ and $\xi_2 = \int_0^V I\Delta T \, dv$.

Here, it is worth noting the differences in absorbed laser energy distribution between the three energy-transport states. For all three lasers (CW, ns, and ps), the incoming incident photon energy E = 2.33 eV is greater than the bandgap energy of monolayer WSe_2 E_g = 1.67 eV.[32] Photoexcited electrons lose this excess energy ($E - E_g$) by direct phonon emission during fast thermalization adding to the nonradiative energy contribution in the sample. The majority of these photoexcited electrons then recombine with the holes across the bandgap E_g via nonradiative recombination. However, a finite percentage of the excited electrons recombine radiatively by emitting photons. We will define the percentage of absorbed photon energy ascribed to radiative recombination of electrons−hole pairs as βE_g where β is the radiative recombination efficiency. Therefore, during laser excitation, the total absorbed energy converted to nonradiative processes becomes $E - E_g + (1 - \beta)E_g$.

In our picosecond energy-transport state, introducing a picosecond pulsed laser (13 ps laser pulse width) distinguishes the nonradiative recombination heating effect $(1 - \beta)E_g$ from the fast thermalization energy contribution $E - E_g$ allowing for characterization of the radiative recombination efficiency β. This is because the 13 ps pulse width is much shorter than the recombination lifetime of excitons in monolayer WSe_2, which has been observed to be 4 ns.[29] In other words, during the ps laser pulse, the only energy contributed to the system comes from $E - E_g$ converted to thermal energy since radiative recombination has not occurred yet, detailed description is shown Figure 2d. The nonradiative recombination effect from $(1 - \beta)E_g$ has much less of an impact on the accumulated heating of the sample and the measured temperature rise during the picosecond pulse. On the other hand, the CW and ns cases have a greater dependence on the accumulated heating effect from nonradiative recombination. The differentiated energy contributions between the multiple energy-transport mechanisms, steady-state and near-zero transport (Figure 2c), distinguish the radiative recombination effect in the 2D monolayer materials.

To experimentally determine the radiative recombination efficiency, laser heating and Raman probing of the WSe_2 monolayers with the ps laser yield a new Raman shift coefficient ψ_{ps}. This laser power differential can be divided by the CW reference ψ_{CW} to form a normalized RSC: $\Theta_2 = \psi_{ps}/\psi_{CW}$. Note that once again, taking the ratio of these separate Raman shift coefficients eliminates the effect from laser absorption and the Raman temperature coefficient. Therefore, Θ_2 can be equated to the ratio of the temperature rises from CW and ps laser heating: $\Delta T_{ps}/\Delta T_{CW}$.

Next, two distinct numerical simulations of the heat transfer during ps heating are done: one to simulate the temperature rise induced by accumulated heating at the substrate (ΔT_0) and another to simulate the temperature rise in the monolayer sample from a single ps laser pulse (ΔT_1). Since the single ps pulse heating only involves a fractional amount of the total thermal energy involved in overall system heating, it becomes possible to introduce the factor $(E - E_g)/[E - E_g + (1 - \beta)E_g]$ to the temperature rise ΔT_1. This term represents the percentage of thermal energy contribution from direct phonon emission during fast thermalization. Therefore, ΔT_{ps} can be written in terms of the radiative recombination efficiency β and solved for based on the measured ratio Θ_2.

■ RESULTS AND DISCUSSION

Interface Thermal Conductance Determination. A LabView computer program automatically adjusted a neutral density optical filter to vary the laser power eight to twelve times during room-temperature Raman measurements. A charge-coupled-device (CCD) camera (Olympus DP-26, Olympus Optical Co., Ltd.) captured an image of the laser spot on the sample surface. The spatial energy distribution from the incident lasers (CW, ns, and ps) on the sample surface is characterized by a Gaussian function and can be derived from the image data. The laser spot radius is calculated at e^{-1} of the peak intensity. The radius from the image data is used during numerical modeling to simulate as accurately as possible the temperature rise in the sample. The approximate radii for each laser are given as follows: r_0 = 1.9 μm (CW), r_0 = 1.0 μm (ns), and r_0 = 1.6 μm (ps). The slight asymmetry of the laser spot energy distribution (seen in Figure 5d−f) should not impact the final results since the heat conduction occurs

https://dx.doi.org/10.1021/acsami.0c14990
ACS Appl. Mater. Interfaces 2020, 12, 51069−51081

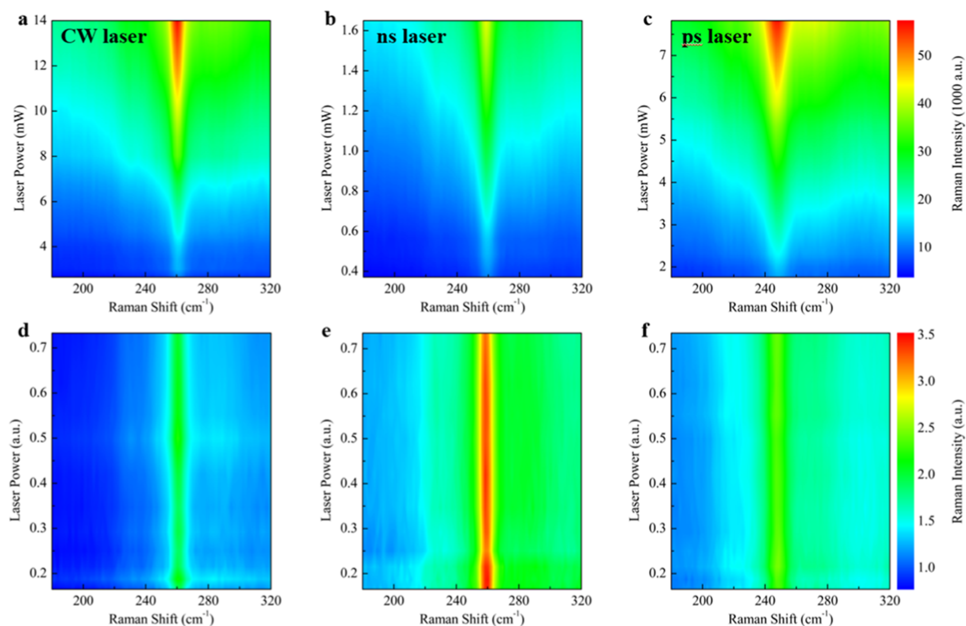

Figure 4. Two-dimensional contours of the laser-dependent peak Raman intensities for the degenerate A_{1g} and $^1E_{2g}$ first-order vibrational modes near 250 cm^{-1}. (a)−(c) show the increasing intensity as the laser power increases for all three laser heating cases: CW, ns, and ps. (d)−(f) Same Raman intensity contours plotted with the laser power normalized across all three laser cases.

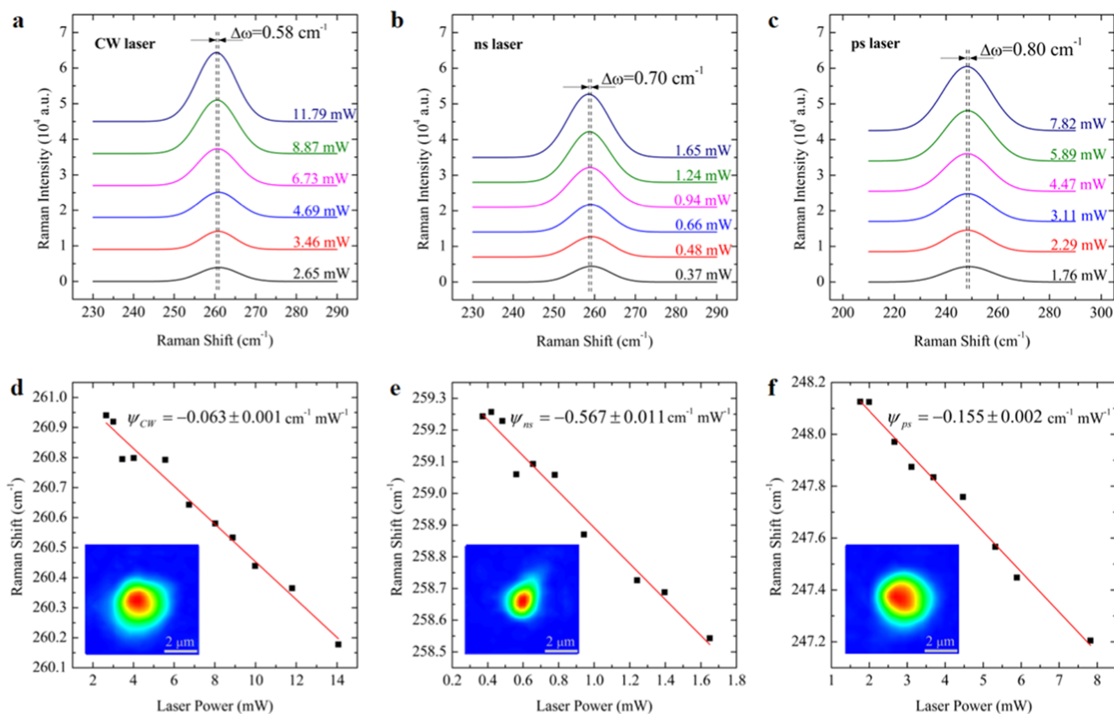

Figure 5. Illustration of the Raman peak location dependency on laser power. (a−c) Six representative Raman spectra as the Gaussian fitted curves applied to the signal at 250 cm^{-1}. The peak location is slightly redshifted as laser power increases by 0.58, 0.70, and 0.80 cm^{-1} for the CW, ns, and ps cases, respectively. Note that each laser heating experiment involves different ranges of laser power to induce measurable Raman signal redshifts. Because the heat conduction and energy input vary between the three laser heating cases, the temperature response of the system will also be different. The laser power ranges are chosen such that the resulting $\Delta\omega$ is between 0.6 and 0.8 cm^{-1}, an optimal redshift range that preserves the linear Raman shift dependence exploited via the ET-Raman method. This range also must be chosen such that the maximum laser power used does not lead to sample damage. (d−f) Raman shift locations of the WSe_2 signal plotted against laser power for all three laser scenarios. Note the negative linear relationship as laser power increases. The slope of the fitted line represents the Raman shift coefficient used to evaluate interfacial thermal resistance and radiative recombination efficiency. The bottom left insets show the Gaussian spatial energy distribution of the laser spot on the sample surface under the 20× objective lens for each respective laser.

radially throughout the sample and the substrate once the laser is incident on the monolayer surface. This radial heat conduction will quickly smooth out the tiny effect of the asymmetric laser intensity distribution. Additionally, the radius

https://dx.doi.org/10.1021/acsami.0c14990
ACS Appl. Mater. Interfaces 2020, 12, 51069−51081

is measured in two perpendicular directions and averaged to more precisely characterize the experimental energy distribution. In the time domain, the three lasers have distinct intensity distributions. The CW laser continuously emits light, while the ns and ps lasers emit light in periodic pulses with defined repetition rates: 300 kHz and 48.2 MHz for the ns and ps lasers, respectively. This translates into a 200 ns pulse width at 3 μs intervals for the ns laser and a 13 ps pulse width at 20.8 ns intervals for the ps.

The laser power incident on the sample after passing through the filter and the 20× objective lens ranged from 2.65 to 14.07 mW; 0.37 to 1.65 mW; and 1.76 to 7.82 mW for the CW, ns, and ps lasers, respectively. Figure 4a−c shows the 2D contour map of WSe_2 Raman peak intensity of a single representative monolayer sample (sample #5), the sample that will be used to discuss the experimental results (G and β values were evaluated for a total of five samples). The Raman intensity of the degenerate A_{1g} and $^1E_{2g}$ peak increases with laser power. Although the Raman shift change against the laser power is small, this trend is still evident in Figure 4. The normalized laser power contours shown in Figure 4d−f highlight the consistent, dominant Raman peak signal near 250 cm^{-1} for all laser powers.

Note that the ps Raman signal appears slightly more redshifted ($\Delta\omega \sim 10$ cm^{-1}) relative to the CW and ns signals. Due to minor optical alignment issues with the ps laser, the measured Raman signal received inside the spectrometer differs a small amount from the signal collected from the other lasers. Furthermore, the spectrometer is calibrated using the 532 nm CW laser. The emitted wavelength of the ps laser deviates more from the desired 532 nm wavelength (relative to the CW and ns lasers) due to manufacturing issues. This will inevitably impact the absolute measured ps Raman signal. However, because the ET-Raman method solely depends on the relative redshift induced by increasing laser powers, the absolute differences between the lasers should not influence the final results.

To precisely determine the Raman shift change with laser power, accurate determination of the Raman peak location is needed by peak fitting. Six representative room-temperature Raman spectra at different laser powers are shown in Figure 5a−c for all three energy-transport states; they show the small Raman shift change when the laser power is increased from low end to high end. This figure illustrates the Raman peak location redshift at increased laser powers. There is a balance between the experimental accuracy and physics consideration for the Raman shift change. A large Raman shift change is preferred to improve experimental accuracy, and a small temperature rise (Raman shift change) is needed to ensure that the sample does not experience a high-temperature rise that will result in physical property change or structural damage. The overall Raman shift change is controlled to be less than 1 cm^{-1}, in our case around 0.8 cm^{-1} or less. The power-dependent peak positions in the low power range are shown in the figure using $\Delta\omega = \omega(P_2) - \omega(P_1) = \psi(P_2 - P_1)$ where ψ is the RSC. Any aberrations in this linear relationship are derived from the uncertainties in Raman peak Gaussian fittings or the laser heating effect.

Figure 5d−f shows more clearly the linear relationship between Raman shift and laser power. The slope of the linear fitting represents the laser power differential we have denoted as the Raman shift coefficient ψ (i.e., $\partial\omega/\partial P$). The RSC is proportional to the local temperature rise of the sample. Moreover, the RSC represents the local temperature rise for unit laser power irradiation. For the representative sample being discussed, we obtain ψ values of $-(0.063 \pm 0.001)$, $-(0.57 \pm 0.01)$, and $-(0.155 \pm 0.002)$ cm^{-1} mW^{-1} for the CW, ns, and ps cases, respectively. The three types of lasers induce distinct optical heating phenomena, which make each ψ value unique. Furthermore, since each ψ is proportional to the same laser absorption coefficient and Raman temperature coefficient, taking the ratio of any of these RSC values cancels out these sample-dependent variables.

To determine the interfacial thermal conductance, we begin with the normalized ratio of ns RSC to CW RSC: $\Theta_1 = \psi_{ns}/\psi_{CW}$. The normalized RSC Θ_1 becomes a function of local temperature rises of the WSe_2 monolayer sample alone from CW heating and ns heating. Note that the local temperature rises for both the CW and ns cases are Raman intensity weighted averages. In the CW case, this is evaluated as $\overline{T}_{CW} = \int_0^V I\, e^{-z/\tau_L} T\, dv / \int_0^V I\, e^{-z/\tau_L}\, dv$ where I is the laser intensity, T is the temperature at each point, V is the sample volume, and e^{-z/τ_L} represents the intensity attenuation once the light enters the sample. For the monolayer samples studied in this work, such intensity attenuation becomes negligible but will be important for thick (e.g., tens of nanometers) samples. Note that the temperate at any point on the sample is governed by the basic equation relating the temperature difference across an interface to the resistance of heat transfer across it: $T_{WSe_2} = R''_{tc}q'' + T_{SiO_2}$ where q'' is local heat flux at the interface and T_{SiO_2} is the substrate surface temperature. Due to the extremely thin thickness of the sample, the in-plane heat conduction and hot carrier diffusion effect are negligible compared with the local interface energy transport. Thus, it can be shown that the Raman intensity weighted average reduces to $\overline{T}_{CW} = aR''_{tc}I_0/2 + \overline{T}_{s,CW}$ where R''_{tc} is the interfacial thermal resistance, a is the laser absorption, I_0 is the incoming laser peak intensity (assuming unit 1 mW irradiation where the laser intensity has a Gaussian distribution of $I = I_0 \exp(-r^2/r_0^2)$), and $\overline{T}_{s,CW}$ is the Raman intensity weighted average temperature rise of the substrate under CW heating. In the ns case, the average must be integrated over the space and time domain: $\overline{T}_{ns} = \int_0^t \int_0^V I\, e^{-z/\tau_L} T\, dv\, dt / \int_0^t \int_0^V I\, e^{-z/\tau_L}\, dv\, dt$. This equation can similarly be reduced to $\overline{T}_{ns} = aR''_{tc}I_0/(2\sqrt{2}) + \overline{T}_{s,ns}$ with $\overline{T}_{s,ns}$ as the average temperature rise of the substrate under ns heating and I_0 as the incoming laser intensity for the ns laser. Note that the above weighted averages for temperature rises in both CW and ns cases only involve one unknown: the interfacial thermal resistance R''_{tc}.

The above treatment has significance for the 3D modeling of heat conduction in the sample structure. Since the WSe_2 sample is so thin (∼1 nm), normal modeling would require a large number of meshes and take a very long time to simulate a physically reasonable domain size of ∼10 μm using a variable mesh starting from <1 nm in WSe_2. In our modeling, first of all, we model the heat conduction in the substrate to obtain its temperature rise under CW and ns laser heating situations ($\overline{T}_{s,CW}$ and $\overline{T}_{s,ns}$) with surface heat flux boundary conditions. Then, the temperature rise of the WSe_2 layer is calculated using the above equations. In the modeling, the optical absorption depth of WSe_2 is calculated using $\tau_L = \lambda/4\pi k_L$ where $\lambda = 532$ nm is the laser wavelength and the extinction

https://dx.doi.org/10.1021/acsami.0c14990
ACS Appl. Mater. Interfaces 2020, 12, 51069−51081

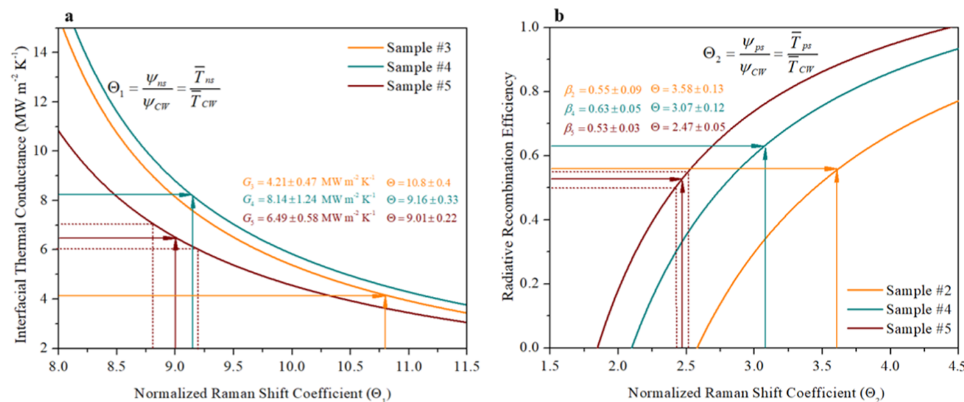

Figure 6. Quantities of interest, interfacial thermal conductance G and radiative recombination efficiency β, behave as functions of their respective normalized Raman shift coefficient. The experimentally determined Θ_1 and Θ_2 identify the corresponding material property. Sample #5 displays the uncertainty values for both G and β. (a) For the measured RSC $\Theta_1 = 9.01 \pm 0.22$ of sample #5 (i.e., the ratio of ns temperature rise to CW temperature rise), the corresponding G value is 6.49 ± 0.58 MW m^{-2} K^{-1}. (b) For the measured RSC of $\Theta_2 = 2.47 \pm 0.05$ (i.e., the ratio of ps temperature rise to CW temperature rise), the corresponding radiative recombination efficiency is $\beta = 0.53 \pm 0.03$.

Table 1. Raman Shift Laser Power Coefficients (RSC) for the CW and ns Cases along with the Normalized RSC and Corresponding Interfacial Thermal Conductance

sample number	ψ_{CW} (cm^{-1} mW^{-1})	ψ_{ns} (cm^{-1} mW^{-1})	Θ_1	G (MW m^{-2} K^{-1})
1	−0.064 ± 0.002	−0.36 ± 0.03	5.61 ± 0.23	15.9 ± 5.0
2	−0.052 ± 0.001	−0.57 ± 0.01	11.0 ± 0.3	2.10 ± 0.14
3	−0.051 ± 0.002	−0.55 ± 0.01	10.8 ± 0.4	4.21 ± 0.47
4	−0.056 ± 0.002	−0.51 ± 0.01	9.16 ± 0.33	8.14 ± 1.24
5	−0.063 ± 0.001	−0.57 ± 0.01	9.01 ± 0.22	6.49 ± 0.58

coefficient $k_L = 1.28$ is used from reference values.[33,34] Note that the accuracy of the absorption depth will not affect the final interface thermal conductance determination since the absorption coefficient is canceled out during the temperature rise ratio calculation. Then, since ψ_{CW} and ψ_{ns} are proportional to the average temperature rises of the WSe_2 monolayer sample under each laser heating scenario, the normalized RSC $\Theta_1 = \psi_{ns}/\psi_{CW}$ can be equated to the temperature rise ratio $\overline{T}_{ns}/\overline{T}_{CW}$. Thus, the interfacial thermal resistance becomes entirely dependent on the experimentally determined Θ_1. The only other relevant parameters used in modeling are the volumetric heat capacities of WSe_2 ($\rho c_p = 1.98 \times 10^6$ J m^{-3} K^{-1}) and glass ($\rho c_p = 1.65 \times 10^6$ J m^{-3} K^{-1}) as well as the thermal conductivity of glass ($k = 1.4$ W m^{-1} K^{-1}).[31,35]

For sample #5, the normalized RSC is evaluated as $\Theta_1 = 9.01 \pm 0.22$. Figure 6a shows how Θ_1 changes with interfacial thermal conductance. With the experimentally measured ratio Θ_1, we can precisely determine the corresponding interfacial conductance G. For the given value of Θ_1, the interfacial thermal conductance is 6.49 ± 0.58 MW m^{-2} K^{-1}. The uncertainty determination based on the uncertainty of Θ_1 is also included in Figure 6a. In this work, we have measured five samples. The results for G along with the relevant parameters are summarized in Table 1.

Radiative Recombination Efficiency Determination. Once the interfacial thermal conductance has been determined, we apply the ps Raman shift coefficient ψ_{ps} to determine the radiative recombination efficiency β. For the sample under discussion (sample #5), $\psi_{ps} = -(0.155 \pm 0.002)$ cm^{-1} mW^{-1}. The normalized RSC taken as $\Theta_2 = \psi_{ps}/\psi_{CW}$ becomes 2.47 ± 0.05. This ratio is equivalent to the ratio of Raman intensity weighted temperature rises calculated from numerical modeling: $\overline{T}_{ps}/\overline{T}_{CW}$. It is important to note that $\overline{T}_{ps}$ is composed of numerical temperature rises from (1) accumulated steady-state heating at the substrate interface (ΔT_0) and (2) single-pulse near-zero transport heating in the WSe_2 monolayer (ΔT_1). The accumulated temperature rise of the substrate is calculated, assuming 1 mW unit laser power irradiation. The absorbed laser energy is converted to thermal energy with a percentage of $[E - E_g + (1 - \beta)E_g]/E$ in the physical process. Here, E is the laser photon energy (2.33 eV) and E_g is the WSe_2 bandgap (1.67 eV). CW and ns simulations similarly assume 1 mW laser irradiation with the same thermal energy contribution. Note that the 1 mW laser irradiation assumption for the simulations is feasible and does not affect our results because we take the ratio of temperature rises to form the RSC.

Considering the single ps pulse heating effect, the atomically thin monolayer WSe_2 will not have 1 mW laser absorption. This is because the optical absorption depth of monolayer WSe_2 ($\tau_L = 33$ nm) is much greater than the sample thickness ($\Delta z = 0.7$ nm); only a small fraction of the 1 mW unit laser power is absorbed in the sample. It is important to note that the absorbed energy can only be converted to thermal energy $E - E_g$ because it occurs at the timescale of the 13 ps pulse, much earlier than e−h recombination. Thus, the temperature rise from single-pulse heating ΔT_1 results from a percentage of the absorbed laser energy as $(E - E_g)/E$.

Note that the thickness of single-layer WSe_2 has been reported as ~0.7[36] and ~1.1 nm[37] based on AFM measurements. In our modeling, we use the former value because it matches our own AFM measurement. We could have easily chosen the latter since sample thickness dependence is nullified during Raman shift coefficient ratio analysis. The combined heating effect due to accumulated and pulse heating can then be summarized by the overall temperature rise $\overline{T}_{ps} = \Delta T_0 +$

https://dx.doi.org/10.1021/acsami.0c14990
ACS Appl. Mater. Interfaces 2020, 12, 51069−51081

Table 2. Raman Shift Coefficients for the CW and ps Cases along with the Normalized RSC and Corresponding Radiative Recombination Efficiency β

sample number	ψ_{CW} (cm^{-1} mW^{-1})	ψ_{ps} (cm^{-1} mW^{-1})	Θ_2	β
1	−0.064 ± 0.002	−0.120 ± 0.002	1.89 ± 0.06	0.36 ± 0.06
2	−0.052 ± 0.001	−0.186 ± 0.005	3.58 ± 0.13	0.55 ± 0.09
3	−0.051 ± 0.002	−0.162 ± 0.004	3.18 ± 0.12	0.65 ± 0.07
4	−0.056 ± 0.002	−0.171 ± 0.004	3.07 ± 0.12	0.63 ± 0.05
5	−0.063 ± 0.001	−0.155 ± 0.002	2.47 ± 0.05	0.53 ± 0.03

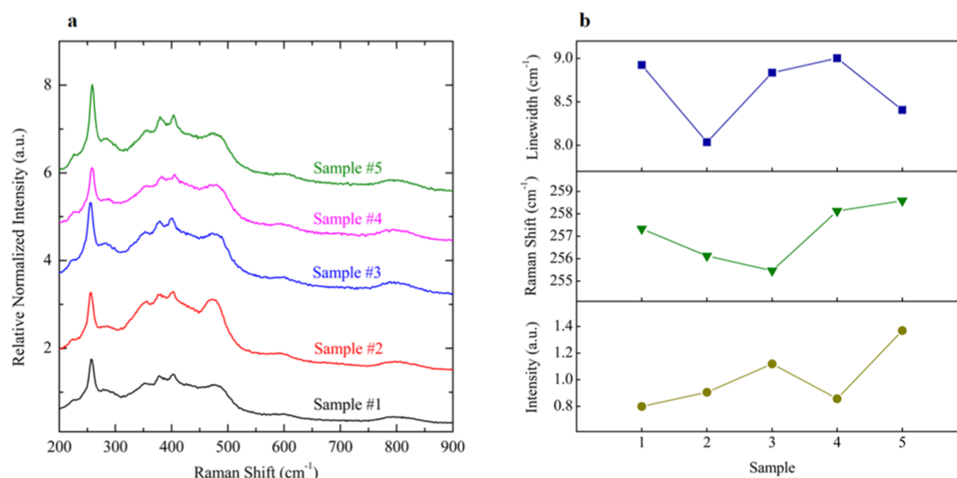

Figure 7. Raman spectra comparison of all five samples from ns laser probing. (a) Plotted Raman spectra where the intensity axis is normalized to account for laser power and integration time, both slightly adjusted over the course of ET-Raman measurements to extract a reliable Raman shift coefficient. (b) Peak intensity, Raman shift location, and linewidth of the WSe_2 Raman signal for each sample. Note that the WSe_2 characteristic peak around 250 cm^{-1} is not identical across the five monolayer samples. Direct comparison of the Raman signal characteristics illustrates the unique structural composition of each sample. The maximum percent difference across all five samples is 53% for peak intensity, 11% for linewidth, and 1.2% for Raman shift. The moderate differences between the samples suggest that the crystal structure and interface bonding are not identical, which would lead to slight differences in interfacial thermal conductance and radiative recombination efficiency.

ΔT_1 where β is the only unknown. Finally, β can be solved for based on the experimentally measured ratio Θ_2. For the sample (sample #5) being considered, Θ_2 = 2.47 ± 0.05, which corresponds to a radiative recombination efficiency of 0.53 ± 0.03. The results for all five samples are shown in Table 2. Figure 6b demonstrates how the normalized RSC Θ_2 changes for different values of β. The experimentally measured Θ_2 identifies the radiative recombination efficiency of the WSe_2 sample. The uncertainty determination for β is also shown in the figure.

As can be seen in the tables, there is some slight variation between the measured G and β values for the five monolayer samples. Due to stage drift and the atomic-level thickness of the samples, the focal plane of the laser on the sample was not always the same during laser heating and Raman probing. This leads to slight inconsistencies in the location of the Raman shift signal, which ultimately determines the laser power differential ψ. However, any inconsistencies will be factored out during the ratio analysis. The greatest source of uncertainty arises from the linear fitting itself. As evident in Figure 3d−f, not all data points match the fitting exactly. This linear fitting is based on the Raman peak positions of the Gaussian fitted curves applied to the degenerate vibrational modes near 250 cm^{-1}. These theoretical curves are subject to non-negligible error that could impact the resulting G and β values.

Physics Interpretation of the Measured Interface Thermal Conductance. Many studies have explored interfacial thermal transport between MoS_2 and various substrates, including SiO_2. Less research has been devoted to the interfacial thermal conductance of WSe_2-based 2D structures. Vaziri et al. explored interface thermal conductance between heterogeneously layered 2D materials using Raman thermometry.[38] In a heterostructure stack of single-layer graphene on top of a WSe_2 monolayer resting on a SiO_2 substrate, they observed thermal conductance across the WSe_2/SiO_2 interface to be 15 ± 4 MW m^{-2} K^{-1}. Another study by Behranginia et al. examined the energy dissipation in few-layered WSe_2 field-effect transistors with thickness ~7 nm.[39] Using low-frequency Raman thermometry and density functional perturbation theory (DFPT) to model phonon dispersion, they predict an interface thermal conductance between single-layer WSe_2 and SiO_2 substrate as ~13 MW m^{-2} K^{-1}. These results are in close agreement with the measured G value for sample #1 in our own experiments (G = 15.9 ± 7.0 MW m^{-2} K^{-1}) and within a reasonable distance from the range of our other measured G values (2−8 MW m^{-2} K^{-1}) for samples #2−5.

One possible explanation for the larger interfacial thermal conductance of sample #1, a noticeable outlier relative to the other samples, stems from laser heating damage at the beginning of Raman measurements. Structural changes in the sample induced by overheating could skew Raman peak location and intensity. Because the ET-Raman method depends on relative Raman shift location and Gaussian fitted curves, the resulting Raman shift coefficient would then carry non-negligible variation compared to that of an undamaged sample. Therefore, it is suspected that the larger, maximum laser power used during CW Raman measurements for sample

https://dx.doi.org/10.1021/acsami.0c14990
ACS Appl. Mater. Interfaces 2020, 12, 51069−51081

#1 (∼30 mW) compared to that of the other four samples (10−14 mW) altered the structural composition of the WSe_2 monolayer flake leading to a larger G value and uncertainty.

Furthermore, the sample-to-sample structure difference would explain the variation in interfacial thermal conductance between the five samples. Slight differences in the Raman spectrum between the samples highlight the underlying sample structure diversity. The Raman spectrum of all five samples from ns laser probing is shown in Figure 7a. The spectra shown are normalized for laser power and integration time. Note that the relative peak intensity of the 250 cm^{-1} signal is not uniform across all five samples. More detailed analysis of the Raman peak characteristics for all five samples is shown in Figure 7b. This figure shows the Raman shift location, linewidth, and peak intensity of the signal for each measured monolayer. The peak intensity shows the most variation. This is most likely from distinct Raman intensity enhancement at the interfacial gap of each individual monolayer sample; varying atomic-scale distances between the bottom of the monolayer and the top of the substrate will cause different levels of interference for the light entering and reflecting within the interfacial gap. Therefore, the intensity variation between the samples is an indicator of interfacial spacing variation. Dissimilar spacing in this region across all five samples leads to distinct interfacial thermal transport, which explains the modest range of values reported in this work. General uncertainty introduced by the ET-Raman system itself (primarily from Raman peak fitting) will also lead to minimal discrepancies between reported G values. However, the effect from sample-to-sample differences largely outweighs the effect of general uncertainty from the measurement technique.

Comparing experimentally measured interfacial thermal conductance values with the peak intensity data from Figure 5b reveals a relation between the samples with the lowest Raman intensity and the highest conductance (samples #1 and #4). This makes sense because the larger conductance values will have small resistance and better interfacial contact. Less spacing between the substrate and monolayer means that the Raman intensity enhancement due to reflections within the interfacial gap is reduced and the resulting intensity decreases. This relation between peak intensity and G does not hold true for the other three samples because the inherent structural properties of the WSe_2 crystal also play a critical role in Raman signal intensity.

The linewidth also shows moderate sample dependency. The Raman signal linewidth is related to the phonon lifetime with larger linewidths corresponding to shorter lifetimes and smaller linewidths corresponding to longer lifetimes. Because phonon lifetime is related to grain size in the crystal structure, the slight variation in linewidth suggests that each sample could have marginally different structural compositions. The Raman shift changes between each sample show the least amount of variation. The sample diversity implies a sensible range of interface bonding strengths and crystal structures, which would explain the marginal range of interfacial thermal conductance values reported in this work.

For comparison, it is also worth discussing interfacial transport characteristics of similar 2D materials such as MoS_2 and WS_2. Yalon et al. observed an interfacial thermal conductance of ∼15 MW m^{-2} K^{-1} for chemical vapor deposition (CVD)-grown monolayer MoS_2 flakes on the SiO_2 substrate at room temperature via Raman thermometry.[19] However, the difficulty of direct laser absorption measurements due to multiple light reflections at interfacial gaps required an estimation of absorption, which could lead to unknown uncertainty in those final measurements. Another study by Yalon et al. using a similar Raman-based approach shows interface thermal conductance between monolayer MoS_2 and SiO_2 as 14 ± 4 MW m^{-2} K^{-1}.[40] Yu et al. used Raman thermometry techniques to measure G of 16−17 and 30 MW m^{-2} K^{-1} for the single-crystal MoS_2 and WS_2 monolayers on the sapphire substrate, respectively.[41] They concluded that the strength of the interaction between 2D TMDs and substrates strongly influences the interfacial thermal conductance; transferring as-grown MoS_2 monolayer flakes to a separate sapphire substrate resulted in a 40−50% drop in measured G. The group also observed an interfacial thermal conductance of 18.6 MW m^{-2} K^{-1} for the single-crystal MoS_2 monolayers on the SiO_2/Si substrate.

In all of the aforementioned studies, the radiative recombination of the generated electron−hole pairs has not been considered. The assumption that all of the absorbed energy in the monolayer sample is converted to thermal energy fails to account for the considerable proportion of energy converted to light when the electrons recombine with the holes and release energy through photon emission. Thus, this overestimated absorbed energy would lead to larger interfacial thermal conductance values. The ET-Raman method circumvents this problem of overestimated energy absorption by nature of the ratio analysis through which the absorbed laser energy is canceled out. This explains the lower range of the conductance value results determined in this study.

Furthermore, most studies explore interfacial conductance between the TMD monolayers and thermally grown silicon dioxide substrate. Fewer studies have been done with the fused silica substrates. Thermally grown silicon dioxide has smaller surface roughness relative to fused silica. To illustrate this point, fused silica root mean square (RMS) surface roughness (δ) measures 0.4 nm after a combination of washing with basic peroxide and then acidic peroxide.[42] Additionally, even after CO_2 laser polishing, fused silica has a measured surface roughness (R_a) up to 25 nm.[43] For comparison, in the Si/SiO_2 substrates, as oxide growth reaches 10 nm thickness during oxidation, surface roughness (δ) reaches a maximum around 0.12 nm.[44] The minimum possible difference between these reported roughness values is 28% of the WSe_2 monolayer thickness, meaning surface roughness effects become much more pronounced at the atomic scale. It has been well documented that surface roughness decreases overall thermal transport across an interface.[9] This is because when the RMS roughness δ becomes larger than the phonon wavelength, interface roughness more strongly affects phonon transport.[45] In other words, when the phonon wavelength is larger than the interface roughness, the phonon can pass through the rough region as if it were not present. Phonons with wavelengths smaller than δ are more likely to attenuate passing through the interface. Therefore, the greater surface roughness of the fused silica substrate used in our samples would also explain the lower range of interfacial thermal conductance values reported in this work.

In our previous works, we demonstrated an order of magnitude difference in interface thermal conductance in few-layered MoS_2 due to interface surface effects. Applying the ET-Raman technique to characterize seven MoS_2 samples (6.6−17.4 nm) on c-Si, the interfacial thermal conductance values were measured in the range of 5−8 MW m^{-2} K^{-1}.[28] Similar

https://dx.doi.org/10.1021/acsami.0c14990
ACS Appl. Mater. Interfaces 2020, 12, 51069−51081

sized MoS_2 samples ranging from 1.8 to 18.0 nm supported by an unpolished glass substrate were reported to have interfacial thermal conductance values in the order of ∼0.5 MW m^{-2} K^{-1}.[46] This 1 order of magnitude difference can be explained by the imperfect contact between the unpolished glass and the 2D material. When the MoS_2 sample is loosely supported by the high points of the glass substrate, the interfacial thermal conductance decreases. A 2D sample supported by a less rough substrate surface such as c-Si enhances interface energy coupling due to the better contact between the adjacent materials leading to larger *G* values. These examples support our claim that relatively rough substrate surfaces, such as the fused silica in our experiments, can dramatically lower interfacial thermal conductance.

Discussions on Electron−Hole Radiative Recombination. The radiative recombination efficiency, also known as internal quantum efficiency (IQE) or photoluminescence quantum yield (PL QY), of TMD 2D materials has received significant attention because of the enhanced photoluminescence as single atomic layers. Salehzadeh et al. observed an IQE of 8.3% in mechanically exfoliated single-layer MoS_2 on the Si/SiO_x substrate at room temperature via power-dependent photoluminescence studies and rate equation analysis.[47] They determine that Shockley−Read−Hall recombination and indirect Auger scattering reduce the maximum allowable IQE for MoS_2 light-emitting devices. Liu et al. observed an IQE of 6.35% for single-layer CVD-synthesized WS_2 on the sapphire substrate through transient absorption measurements under pulsed laser irradiation.[48] In addition, it has been shown that as-exfoliated and as-grown CVD-synthesized WSe_2 monolayers on the fused silica substrate exhibit a quantum yield of ∼2%.[49]

Other works have detailed how to increase the PL QY of monolayer TMDs through chemical treatment or electrostatic doping. Amani et al. developed an organic superacid treatment using bis(trifluoromethane) sulfonimide (TFSI) to vastly improve the PL QY of sulfur-based single-layer TMDs on quartz substrates to near unity performance.[50] Before treatment, they found the maximum quantum yield of the as-exfoliated monolayers to be at or below 5% for MoS_2, WSe_2, and $MoSe_2$ and at nearly 20% for WS_2. Lien et al. discovered that electrical suppression of the nonradiative pathways via electrostatic doping increases radiative recombination in MoS_2 and WS_2 while decreasing quantum yield for WSe_2.[5151] Before doping, they measured a quantum yield of 8% for single-layer WSe_2. These experiments were done on the Si/SiO_2 substrates.

It has become clear that interactions at the 2D material−substrate interface significantly influence luminescence efficiency for the TMD monolayers. These effects include induced strain, dielectric screening, and doping, with doping from the substrate as the primary facilitator of defect-assisted nonradiative recombination.[8] Furthermore, the bonding strength between the substrate and 2D material also dictates overall radiative recombination efficiency. Kim et al. demonstrated that strong coupling between the substrate and single-layer WSe_2 diminishes maximum achievable PL QY.[52] Using a solvent evaporation-mediated decoupling (SEMD) technique, an evaporating solvent causes surface tension to release the grown monolayer from the substrate, they observe quantum yield up to ∼60% for the CVD-grown WSe_2 monolayers decoupled from the fused silica substrates. Before decoupling, the same monolayers only exhibited ∼1% PL QY.

The radiative recombination efficiency values reported in this work range from 36 to 65%, larger than the most reported values for the untreated WSe_2 monolayers (below 8%). However, it is important to note the novel method used to synthesize the 2D crystals used in this work. The studies previously mentioned used the CVD-grown WSe_2 monolayers, which have strong interactions with their substrates. Until this time, the radiative recombination efficiency of high-quality laser-assisted synthesized (LAST) TMD crystals has not been measured. Notably, monolayers synthesized via LAST have lower levels of impurities compared to materials grown via CVD.[23]

There exist a handful of techniques to study the uniformity and quality of atomic-scale 2D materials such as Raman mapping[53] and high-resolution transmission electron microscopy (HRTEM).[54] Azam et al. applied ADF-STEM imaging and PL mapping to characterize the quality, stoichiometry, and defect density of multiple LAST monolayers (MoS_2, WS_2, $MoSe_2$, and WSe_2). The resulting images show monolayers of a single-crystalline nature and show no evidence of substantial vacancies, defects, or doping. The high degree of symmetry of the hexagonal crystal structure is also abundantly evident. Clearly, defect-assisted nonradiative recombination will be mitigated in monolayer samples demonstrating this degree of uniformity and purity. Therefore, it is reasonable to assume that the larger radiative recombination efficiencies measured from our experiments could be partially explained by the low-density of impurities in the WSe_2 monolayer flakes. Further analysis of the thermal and optical properties of 2D materials fabricated by other laser-based synthesis methods such as self-limiting laser crystallization (SLLC)[55] would help identify differences between thin-film fabrication techniques.

CONCLUSIONS

In this work, an energy-transport state-resolved Raman (ET-Raman) method was employed to determine the interfacial thermal conductance and radiative recombination efficiency of supported WSe_2 monolayers on the fused silica substrate. This technique constructed and probed steady, nanosecond, and picosecond energy-transport states and was able to distinguish the effect of radiative recombination. It did not require Raman temperature calibration or laser absorption coefficients, which introduce unknown error to the experimental results. Five monolayer samples were irradiated with a CW and ns laser to simultaneously heat the sample and measure the Raman signal. Raman shift power coefficients were derived from the experimental data and used in conjunction with 3D numerical modeling to determine the temperature rise and corresponding interfacial thermal conductance of the samples. The interfacial thermal conductance values range from 2 to 16 MW m^{-2} K^{-1}. The lower range of the reported values in this work was attributed to the decreased interface energy coupling caused by the relatively rough surface of the fused silica substrate and the novel thin-film fabrication method. Furthermore, this work is one of the first to consider the effect of radiative e−h recombination on thermal transport characteristics of monolayer TMDs. Neglecting radiative recombination leads to an overestimation of absorbed laser energy contributing to larger interfacial thermal conductance values. To determine the radiative recombination efficiency, a ps laser was introduced to define a new Raman shift coefficient. The numerical modeling for ps heating accounts for the ultrafast timescale of fast thermalization that precedes e−h recombination. The

https://dx.doi.org/10.1021/acsami.0c14990
ACS Appl. Mater. Interfaces 2020, 12, 51069−51081

determined temperature rise evaluated from modeling is then related to the CW and ps Raman shift coefficients to determine the radiative recombination efficiency. The efficiency values for the five monolayer samples measured in this work range from 36 to 65%. The rate of radiative recombination determined in this work is higher than other reported values for the CVD-grown TMD monolayers. The discrepancy from other works can be explained by the high-quality TMD monolayers fabricated via a novel laser-based synthesis method (LAST); lower levels of impurities in the 2D material restrict pathways for nonradiative recombination while enhancing radiative recombination. Additionally, the weaker coupling between the 2D material and substrate would enhance radiative recombination. Further studies to explore the bonding strength between LAST-synthesized TMD monolayers with their substrate could also help clarify the substantial PL QY reported in this work.

AUTHOR INFORMATION

Corresponding Authors

Masoud Mahjouri-Samani − *Department of Electrical and Computer Engineering, Auburn University, Auburn, Alabama 36849, United States;* orcid.org/0000-0002-6080-7450; Email: mzm0185@auburn.edu

Xinwei Wang − *Department of Mechanical Engineering, Iowa State University, Ames, Iowa 50011, United States;* orcid.org/0000-0002-9373-3750; Email: xwang3@iastate.edu

Authors

Nicholas Hunter − *Department of Mechanical Engineering, Iowa State University, Ames, Iowa 50011, United States*

Nurul Azam − *Department of Electrical and Computer Engineering, Auburn University, Auburn, Alabama 36849, United States*

Hamidreza Zobeiri − *Department of Mechanical Engineering, Iowa State University, Ames, Iowa 50011, United States*

Ridong Wang − *State Key Laboratory of Precision Measuring Technology and Instruments, Tianjin University, Tianjin 300072, P. R. China*

Complete contact information is available at: https://pubs.acs.org/10.1021/acsami.0c14990

Author Contributions

‖N.H., N.A., and H.Z. contributed equally to this work.

Notes

The authors declare no competing financial interest.

Any opinions, findings and conclusions or recommendations expressed in this material are those of the author(s) and do not necessarily reflect the views of the Defense Microelectronics Activity.

ACKNOWLEDGMENTS

Partial support of this work by the National Science Foundation (CBET1930866 and CMMI2032464) and the Defense Microelectronics Activity (DMEA) (HQ072718C0008) is gratefully acknowledged.

REFERENCES

(1) Choi, W.; Choudhary, N.; Han, G. H.; Park, J.; Akinwande, D.; Lee, Y. H. Recent Development of Two-Dimensional Transition Metal Dichalcogenides and Their Applications. *Mater. Today* **2017**, *20*, 116−130.

(2) Ramasubramaniam, A.; Naveh, D.; Towe, E. Tunable Band Gaps in Bilayer Transition-Metal Dichalcogenides. *Phys. Rev. B: Condens. Matter Mater. Phys.* **2011**, *84*, No. 205325.

(3) Nan, H.; Wang, Z.; Wang, W.; Liang, Z.; Lu, Y.; Chen, Q.; He, D.; Tan, P.; Miao, F.; Wang, X.; Wang, J.; Ni, Z. Strong Photoluminescence Enhancement of MoS_2 through Defect Engineering and Oxygen Bonding. *ACS Nano* **2014**, *8*, 5738−5745.

(4) Wang, H.; Yu, L.; Lee, Y.; Shi, Y.; Hsu, A.; Chin, M.; Li, L.; Dubey, M.; Kong, J.; Palacios, T. Integrated Circuits Based on Bilayer MoS_2 Transistors. *Nano Lett.* **2012**, *12*, 4674−4680.

(5) Salehi, S.; Saffarzadeh, A. Optoelectronic Properties of Defective MoS_2 and WS_2 Monolayers. *J. Phys. Chem. Solids* **2018**, *121*, 172−176.

(6) Zibouche, N.; Kuc, A.; Musfeldt, J.; Heine, T. Transition-metal Dichalcogenides for Spintronic Applications. *Ann. Phys.* **2014**, *526*, 395−401.

(7) Yoon, Y.; Ganapathi, K.; Salahuddin, S. How Good Can Monolayer MoS_2 Transistors Be? *Nano Lett.* **2011**, *11*, 3768−3773.

(8) Yu, Y.; Yu, Y.; Xu, C.; Cai, Y.; Su, L.; Zhang, Y.; Zhang, Y.-W.; Gundogdu, K.; Cao, L. Engineering Substrate Interactions for High Luminescence Efficiency of Transition-Metal Dichalcogenide Monolayers. *Adv. Funct. Mater.* **2016**, *26*, 4733−4739.

(9) Hopkins, P. Thermal Transport across Solid Interfaces with Nanoscale Imperfections: Effects of Roughness, Disorder, Dislocations, and Bonding on Thermal Boundary Conductance. *ISRN Mech. Eng.* **2013**, *1*, 1.

(10) Yasaei, P.; Foss, C. J.; Karis, K.; Behranginia, A.; El-Ghandour, A. I.; Fathizadeh, A.; Olivares, J.; Majee, A. K.; Foster, C. D.; Khalili-Araghi, F.; Aksamija, Z.; Salehi-Khojin, A. Interfacial Thermal Transport in Monolayer MoS_2- and Graphene-Based Devices. *Adv. Mater. Interfaces* **2017**, *4*, No. 1700334.

(11) Zhang, X.; Sun, D.; Li, Y.; Lee, G.-H.; Cui, X.; Chenet, D.; You, Y.; Heinz, T. F.; Hone, J. C. Measurement of Lateral and Interfacial Thermal Conductivity of Single- and Bilayer MoS_2 and MoSe2 Using Refined Optothermal Raman Technique. *ACS Appl. Mater. Interfaces* **2015**, *7*, 25923−25929.

(12) Little, W. A. The Transport of Heat between Dissimilar Solids at Low Temperatures. *Can. J. Phys.* **1959**, *37*, 334−349.

(13) Swartz, E. T.; Pohl, R. O. Thermal Boundary Resistance. *Rev. Mod. Phys.* **1989**, *61*, 605−668.

(14) Zhan, T.; Minamoto, S.; Xu, Y.; Tanaka, Y.; Kagawa, Y. Thermal Boundary Resistance at Si/ Ge Interfaces by Molecular Dynamics Simulation. *AIP Adv.* **2015**, *5*, No. 047102.

(15) Correa, G. C.; Foss, C. J.; Aksamija, Z. Interface Thermal Conductance of van der Waals Monolayers on Amorphous Substrates. *Nanotechnology* **2017**, *28*, No. 135402.

(16) Yan, R.; Simpson, J. R.; Bertolazzi, S.; Brivio, J.; Watson, M.; Wu, X.; Kis, A.; Luo, T.; Walker, A. R. H.; Xing, H. G. Thermal Conductivity of Monolayer Molybdenum Disulfide Obtained from Temperature-Dependent Raman Spectroscopy. *ACS Nano* **2014**, *8*, 986−993.

(17) Judek, J.; Gertych, A. P.; Świniarski, M.; Łapińska, A.; Dużyńska, A.; Zdrojek, M. High Accuracy Determination of the Thermal Properties of Supported 2D Materials. *Sci. Rep.* **2015**, *5*, No. 12422.

(18) Cai, W.; Moore, A. L.; Zhu, Y.; Li, X.; Chen, S.; Shi, L.; Ruoff, R. S. Thermal Transport in Suspended and Supported Monolayer Graphene Grown by Chemical Vapor Deposition. *Nano Lett.* **2010**, *10*, 1645−1651.

(19) Yalon, E.; Aslan, O. B.; Smithe, K. K. H.; McClellan, C. J.; Suryavanshi, S. V.; Xiong, F.; Sood, A.; Neumann, C. M.; Xu, X.; Goodson, K. E.; Heinz, T. F.; Pop, E. Temperature-Dependent Thermal Boundary Conductance of Monolayer MoS_2 by Raman Thermometry. *ACS Appl. Mater. Interfaces* **2017**, *9*, 43013−43020.

(20) Xu, S.; Fan, A.; Wang, H.; Zhang, X.; Wang, X. Raman-Based Nanoscale Thermal Transport Characterization: A Critical Review. *Int. J. Heat Mass Transfer* **2020**, *154*, No. 119751.

(21) Yuan, P.; Li, C.; Xu, S.; Liu, J.; Wang, X. Interfacial Thermal Conductance Between Few to Tens of Layered-MoS_2 and c-Si: Effect of MoS2 Thickness. *Acta Mater.* **2017**, *122*, 152−165.

(22) Splendiani, A.; Sun, L.; Zhang, Y.; Li, T.; Kim, J.; Chim, C.-Y.; Galli, G.; Wang, F. Emerging Photoluminescence in Monolayer MoS_2. *Nano Lett.* **2010**, *10*, 1271−1275.
(23) Azam, N.; Ahmadi, Z.; Yakupoglu, B.; Elafandi, S.; Tian, M. K.; Boulesbaa, A.; Mahjouri-Samani, M. Accelerated Synthesis of Atomically-Thin 2D Quantum Materials by a Novel Laser-Assisted Synthesis Technique. *2D Mater.* **2020**, *7*, No. 015014.
(24) Yuan, P.; Wang, R.; Wang, T.; Wang, X.; Xie, Y. Nonmonotonic Thickness-dependence of In-plane Thermal Conductivity of Few-layered MoS_2: 2.4 to 37.8 nm. *Phys. Chem. Chem. Phys.* **2018**, *20*, 25752−25761.
(25) Zobeiri, H.; Wang, R.; Zhang, Q.; Zhu, G.; Wang, X. Hot Carrier Transfer and Phonon Transport in Suspended nm WS_2 Films. *Acta Mater.* **2019**, *175*, 222−237.
(26) Wang, R.; Wang, T.; Zobeiri, H.; Yuan, P.; Deng, C.; Yue, Y.; Xu, S.; Wang, X. Measurement of the Thermal Conductivities of Suspended MoS_2 and $MoSe_2$ by Nanosecond ET-Raman without Temperature Calibration and Laser Absorption Evaluation. *Nanoscale* **2018**, *10*, 23087.
(27) Zobeiri, H.; Wang, R.; Wang, T.; Lin, H.; Deng, C.; Wang, X. Frequency-Domain Energy Transport State-Resolved Raman for Measuring the Thermal Conductivity of Suspended Nm-Thick $MoSe_2$. *Int. J. Heat Mass Transfer* **2019**, *133*, 1074−1085.
(28) Yuan, P.; Wang, R.; Tan, H.; Wang, T.; Wang, X. Energy Transport State Resolved Raman for Probing Interface Energy Transport and Hot Carrier Diffusion in Few-Layered MoS_2. *ACS Photonics* **2017**, *4*, 3115−3129.
(29) Mouri, S.; Miyauchi, Y.; Toh, M.; Zhao, W.; Eda, G.; Matsuda, K. Nonlinear Photoluminescence in Atomically Thin Layered WSe_2 Arising from Diffusion-Assisted Exciton-Exciton Annihilation. *Phys. Rev. B: Condens. Matter Mater. Phys.* **2014**, *90*, No. 155449.
(30) Zhao, W.; Ghorannevis, Z.; Amara, K. K.; Pang, J. R.; Toh, M.; Zhang, X.; Kloc, C.; Tan, P. H.; Eda, G. Lattice Dynamics in Mono- and Few-layer Sheets of WS_2 and WSe_2. *Nanoscale* **2013**, *5*, 9677−9683.
(31) Incropera, F. P.; DeWitt, D. P. *Introduction to Heat Transfer*; John Wiley & Sons: New York, 2002.
(32) Gusakova, J.; Wang, X.; Shiau, L. L.; Krivosheeva, A.; Shaposhnikov, V.; Borisenko, V.; Gusakov, V.; Tay, B. K. Electronic Properties of Bulk and Monolayer TMDs: Theoretical Study Within DFT Framework (GVJ-2e Method). *Phys. Status Solidi A* **2017**, *214*, No. 1700218.
(33) Jung, G.-H.; Yoo, S.; Park, Q.-H. Measuring the Optical Permittivity of Two-dimensional Materials without a priori Knowledge of Electronic Transitions. *Nanophotonics* **2018**, *8*, 263−270.
(34) Liu, H.-L.; Shen, C.-C.; Su, S.-H.; Hsu, C.-L.; Li, M.-Y.; Li, L.-J. Optical Properties of Monolayer Transition Metal Dichalcogenides Probed by Spectroscopic Ellipsometry. *Appl. Phys. Lett.* **2014**, *105*, No. 201905.
(35) Blinder, A.; Bolgar, A.; Trofimova, Z. A. Thermodynamic Properties of Selenides of Transition Metals. *Powder Metall. Met. Ceram.* **1993**, *32*, 234−239.
(36) Fang, H.; Chuang, S.; Chang, T. C.; Takei, K.; Takahashi, T.; Javey, A. High-Performance Single Layered WSe_2 p-FETs with Chemically Doped Contacts. *Nano Lett.* **2012**, *12*, 3788−3792.
(37) Pawbake, A. S.; Pawar, M. S.; Jadkar, S. R.; Late, D. J. Large Area Chemical Vapor Deposition of Monolayer Transition Metal Dichalcogenides and their Temperature Dependent Raman Spectroscopy Studies. *Nanoscale* **2016**, *8*, 3008.
(38) Vaziri, S.; Yalon, E.; Rojo, M. M.; Suryavanshi, S. V.; Zhang, H.; McClellan, C. J.; Bailey, C. S.; Smithe, K. K. H.; Gabourie, A. J.; Chen, V.; Deshmukh, S.; Bendersky, L.; Davydov, A. V.; Pop, E. Ultrahigh Thermal Isolation across Heterogeneously Layered Two-dimensional Materials. *Sci. Adv.* **2019**, *5*, No. eaax1325.
(39) Behranginia, A.; Hemmat, Z.; Majee, A. K.; Foss, C. J.; Yasaei, P.; Aksamija, Z.; Salehi-Khojin, A. Power Dissipation of WSe_2 Field-Effect Transistors Probed by Low-Frequency Raman Thermometry. *ACS Appl. Mater. Interfaces* **2018**, *10*, 24892−24898.
(40) Yalon, E.; McClellan, C. J.; Smithe, K. K. H.; Rojo, M. M.; Xu, R. L.; Suryavanshi, S. V.; Gabourie, A. J.; Neumann, C. M.; Xiong, F.; Farimani, A. B.; Pop, E. Energy Dissipation in Monolayer MoS_2 Electronics. *Nano Lett.* **2017**, *17*, 3429−3433.
(41) Yu, Y.; Minhaj, T.; Huang, L.; Yu, Y.; Cao, L. In-Plane and Interfacial Thermal Conduction of Two-Dimensional Transition-Metal Dichalcogenides. *Phys. Rev. Appl.* **2020**, *13*, No. 034059.
(42) Henke, L.; Nagy, N.; Krull, U. J. An AFM Determination of the Effects on Surface Roughness caused by Cleaning of Fused Silica and Glass Substrates in the Process of Optical Biosensor Preparation. *Biosens. Bioelectron.* **2002**, *17*, 547−555.
(43) Zhao, L.; Cheng, J.; Chen, M.; Yuan, X.; Liao, W.; Liu, Q.; Yang, H.; Wang, H. Formation Mechanism of a Smooth, Defect-free Surface of Fused Silica Optics using Rapid CO_2 Laser Polishing. *Int. J. Extreme Manuf.* **2019**, *1*, No. 035001.
(44) Ohsawa, K.; Hayashi, Y.; Hasunuma, R.; Yamabe, K. Roughness Increase on Surface and Interface of SiO_2 Grown on Atomically Flat Si (111) Terrace. *J. Phys.: Conf. Ser.* **2009**, *191*, No. 012031.
(45) Hopkins, P. E.; Duda, J. C.; Petz, C. W.; Floro, J. A. Controlling Thermal Conductance through Quantum Dot Roughening at Interfaces. *Phys. Rev. B: Condens. Matter Mater. Phys.* **2011**, *84*, No. 035438.
(46) Yuan, P.; Tan, H.; Wang, R.; Wang, T.; Wang, X. Very Fast Hot Carrier Diffusion in Unconstrained MoS_2 on a Glass Substrate: Discovered by Picosecond ET-Raman. *RSC Adv.* **2018**, *8*, 12767−12778.
(47) Salehzadeh, O.; Tran, N. H.; Liu, X.; Shih, I.; Mi, Z. Exciton Kinetics, Quantum Efficiency, and Efficiency Droop of Monolayer MoS_2 Light-Emitting Devices. *Nano Lett.* **2014**, *14*, 4125−4130.
(48) Liu, Y.; Li, H.; Zheng, X.; Cheng, X.; Jiang, T. Giant Photoluminescence Enhancement in Monolayer WS_2 by Energy Transfer from $CsPbBr_3$ Quantum Dots. *Opt. Mater. Express* **2017**, *7*, 1327−1334.
(49) Ahn, G. H.; Amani, M.; Rasool, H.; Lien, D.-H.; Mastandrea, J. P.; Ager, J. W., III; Dubey, M.; Chrzan, D. C.; Minor, A. M.; Javey, A. Strain-engineered growth of Two-dimensional Materials. *Nat. Commun.* **2017**, *8*, No. 608.
(50) Amani, M.; Taheri, P.; Addou, R.; Ahn, G. H.; Kiriya, D.; Lien, D.-H.; A. J, W.; Wallace, R. M.; Javey, A. Recombination Kinetics and Effects of Superacid Treatment in Sulfur- and Selenium-Based Transition Metal Dichalcogenides. *Nano Lett.* **2016**, *16*, 2786−2791.
(51) Lien, D.-H.; Uddin, S. Z.; Yeh, M.; Amani, M.; Kim, H.; Ager, J. W., III; Yablonovitch, E.; Javey, A. Electrical Suppression of all Nonradiative Recombination Pathways in Monolayer Semiconductors. *Science* **2019**, *364*, 468−471.
(52) Kim, H.; Ahn, G. H.; Cho, J.; Amani, M.; Mastandrea, J. P.; Groschner, C. K.; Lien, D.-H.; Zhao, Y.; Ager, J. W., III; Scott, M. C.; Chrzan, D. C.; Javey, A. Synthetic WSe_2 Monolayers with High Photoluminescence Quantum Yield. *Sci. Adv.* **2019**, *5*, No. eaau4728.
(53) Kang, K.; Lee, K.-H.; Han, Y.; Gao, H.; Xie, S.; Muller, D. A.; Park, J. Layer-by-Layer Assembly of Two-Dimensional Materials into Wafer-Scale Heterostructures. *Nature* **2017**, *550*, 229−233.
(54) Kang, K.; Xie, S.; Huang, L.; Han, Y.; Huang, P. Y.; Mak, K. F.; Kim, C.-J.; Muller, D.; Park, J. High-Mobility Three-Atom-Thick Semiconducting Films with Wafer-Scale Homogeneity. *Nature* **2015**, *520*, 656−660.
(55) Ahmadi, Z.; Yakupoglu, B.; Azam, N.; Elfandi, S.; Mahjouri-Samani, M. Self-limiting Laser Crystallization and Direct Writing of 2D Materials. *Int. J. Extreme Manuf.* **2019**, *1*, No. 015001.

https://dx.doi.org/10.1021/acsami.0c14990
ACS Appl. Mater. Interfaces 2020, 12, 51069−51081